Available online at www.sciencedirect.com
ScienceDirect
Trans. Nonferrous Met. Soc. China 30(2020) 2639−2649
Transactions of Nonferrous Metals Society of China
www.tnmsc.cn

Tensile resistance, microstructures of intermetallic compounds, and fracture modes of welded steel/aluminum joints produced using laser lap welding

Gui-qian LIU, Xiang-dong GAO, Cong PENG, Xiu-hang LIU, Yi-jie HUANG, Yan-xi ZHANG, De-yong YOU

Guangdong Provincial Welding Engineering Technology Research Center,
Guangdong University of Technology, Guangzhou 510006, China

Received 25 December 2019; accepted 3 June 2020

Abstract: The joining of DP780 steel to Al5052 was conducted by laser lap welding, in which the metal vapor and spatters were monitored by a high-speed camera. A universal testing machine was used to test the mechanical properties of the welded joints, and the changing law of lap tensile resistance with the laser welding parameters was analyzed. Optical microscope and scanning electron microscope were used to observe the macro-structure and micro-structure, respectively. Three different intermetallic compounds (IMCs) phases, i.e. banded Fe_2Al_5, $FeAl_2$ and needle-like $FeAl_3$ were generated at the steel/Al interface on microscopic observation. The aim of this research is to investigate the relationship among the lap tensile resistance, the welding parameters and the failure mode under different energy densities. Experimental results showed that the steel/Al joints have two different fracture modes at low heat input and high heat input. The failures happened along the heat-affected zone of the weld and along the steel/Al joint interface, respectively. And both of the two failure modes are brittle fractures. Additionally, cracks appeared at the fracture interface, and needle-like particle clusters were found in the fracture microstructure.
Key words: laser lap welding; tensile resistance; microstructure; failure modes

1 Introduction

Laser welding is being widely used in material connection due to its high welding speed, small heat affected zone and good weld formation [1,2]. Dissimilar aluminum−steel components have been widely used in aerospace, automotive, and shipbuilding industries. The composite structure can improve fuel efficiency, extend range, and control pollution by reducing structural weight. Because of great differences in physical and chemical properties of aluminum and steel, the high-quality and high-efficiency joining of aluminum−steel dissimilar metals is a difficult point in the welding field [3]. At present, connection methods have been used to study the aluminum−steel composite structure, such as laser brazing [4−6], laser penetration welding [7,8], laser–arc hybrid welding [9,10], friction welding [11], explosion welding [12], magnetic pulse welding [13,14], pulse MIG welding [15], and dual beam laser keyhole welding [16]. The welding/brazing technology provides a great potential for Al/steel joining.

Parameter optimization of laser-based welding is a crucial issue for joint quality. The effect of heat input on microstructure changes and strength was studied through three different laser energy densities [17]. The parameters of laser welding of DC04 low carbon steel and 6016 aluminum alloy were optimized by orthogonal design [18]. This work found that the welding speed had the greatest

Foundation item: Project (51675104) supported by the National Natural Science Foundation of China; Project (202002020068) supported by the Guangzhou Municipal Special Fund Project for Scientific and Technological Innovation and Development, China; Project (2017KCXTD010) supported by the Innovation Team Project, Department of Education of Guangdong Province, China
Corresponding author: Xiang-dong GAO; Tel: +86-13711457326; E-mail: gaoxd@gdut.edu.cn
DOI: 10.1016/S1003-6326(20)65408-5

influence on the quality of the weld joint, and the welded joint of the iron−aluminum dissimilar metal failed along the brittle intermetallic phase. Taguchi-response surface method was applied to optimizing welding parameters for obtaining a high mechanical resistance [19]. In order to suppress the propagation of crack and adjust the formation of IMC interface, an appropriate magnetic field was applied to stabilizing the welding process [20]. The quality of welded joints was improved during the pulsed Nd:YAG laser welding of steel and aluminum alloy [21].

It is well known that the joining of aluminum alloy with steel is one of the most challenging issues due to instability of Fe−Al intermetallic compounds. Some researchers [22−24] have focused on the investigation of Fe−Al IMCs in Al/steel joints. Both intermetallic compounds and fracture modes in different powers of laser welding were analyzed [25]. The Fe_2Al_5 was identified as the main phase in the reaction layer formed at the joint interface [26]. TAN et al [27] made attempts to join Al/steel with Al additions, and they investigated diffusion behavior of Zn element at the Fe−Al interface and its mechanical properties.

In the present study, the relationship among the welding parameters, weld processing and intermetallic compounds was investigated. The relationship between laser welding parameters and lap tensile resistance was studied. The effects of process parameters on microstructure were analyzed. The morphology, defects and causes of tensile shear fracture were then discussed.

2 Experimental

The laser welding was performed by using an IPG 4 kW fiber laser welding system, which is shown in Fig. 1(a). Its model was YLS−4000 and the output light wave was continuous. The wavelength of laser was 1070 nm and the focus spot diameter was 400 μm. The welding robot was driven by a six-axis servo motor. The movement of the test piece was driven by the precision servo motor of the workbench. In the welding process, the aluminum liquid floated up to the surface of the weld, and the aluminum had a high laser reflectivity. To protect the laser head from the reflected laser, the laser beam was set at 10° in the welding direction, and the argon tube was placed at 45° to the vertical direction. The weld specimen was fixed by welding fixture by shims and press plates. An ultraviolet-visible sensing camera was used to obtain the features of metal vapor and spatters, the sampling frequency of the camera was 4000 fps with the 640×480 pixels image resolution. The materials of specimen were DP780 dual phase steel and 5052 aluminum alloy, and the size of DP780 and Al5052 was 150 mm × 110 mm × 2 mm. Laser power (P) was changed from 1.7 to 2.5 kW. The range of the welding speed (S) was from 1.5 to 4.5 m/min. The range of the defocusing distance of laser beam (D) was changed from −3 to 4 mm, and the gas flow rate was set as 20 L/min. The schematic illustration of the focus position is presented in Fig. 1(b). It is the zero defocus when the center of the laser beam is on the surface of the steel. The positive defocus means that the focal position of laser beam is above the top surface of the steel. The negative defocus means that focal position of the laser beam is below the top surface of the steel. The schematic of tensile sample is shown in Fig. 1(c). The detail parameters of laser welding are shown in Table 1.

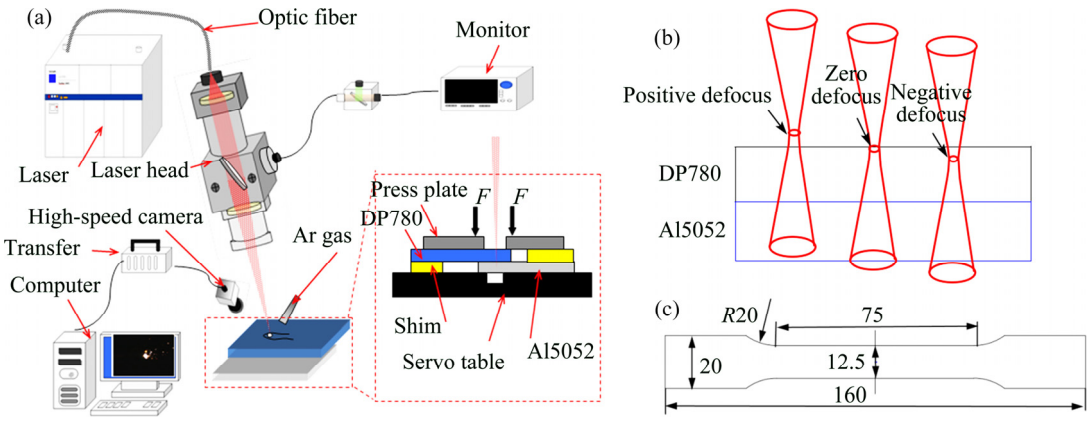

Fig. 1 Schematic diagrams of experiment setup (a), focus positions (b) and tensile sample (c) (unit: mm)

Table 1 Laser welding parameters

Experiment No.	*P*/kW	*S*/(m·min^{-1})	*D*/mm
1	1.7	3	2
2	1.8	3	2
3	1.9	3	2
4	2	3	2
5	2.1	3	2
6	2.2	3	2
7	2.3	3	2
8	2.4	3	2
9	2.5	3	2
10	2.1	1.5	2
11	2.1	2	2
12	2.1	2.5	2
13	2.1	3	2
14	2.1	3.5	2
15	2.1	4	2
16	2.1	4.5	2
17	2.1	3	−3
18	2.1	3	−2
19	2.1	3	−1
20	2.1	3	0
21	2.1	3	1
22	2.1	3	2
23	2.1	3	3
24	2.1	3	4

3 Online monitoring and lap tensile resistance analysis

3.1 Online monitoring

In the welding process, the light, electricity, heat, vision and other signals have the connection with the welding quality. In order to monitor the welding process and evaluate the welding quality, the support vector machine, neural networks and other recognition methods are applied to analyze the welding status through collecting the welding feature information in the welding process. [28−30]. Real-time monitoring of the characteristic information of the laser welding process can accurately and effectively identify the welding status, which is beneficial to improving the welding efficiency. In this case, an ultraviolet and visible sensing high speed camera was used to obtain the features of metal vapor, spatters, and molten pool. Theses features could provide a basis for studying the surface formation of welds and the fracture mode of tensile specimens. As shown in Fig. 2, the laser beam, metal vapor, spatters, molten pool, and reflective shadow of metal vapor could be observed clearly from the original image of the welding process. When the laser power was changed from 2.1 to 2.5 kW, the area of metal vapor became smaller, the number and the size of spatters increased, and the surface of the molten pool became lower. The melting depth of the aluminum side became larger. This indicated that the increase of the inputted welding energy aggravated the stirring reaction of molten steel and aluminum liquid. The defects such as depression, cracks and spatters were more easily formed due to the stirring reaction. To a certain extent, this process contributed the steel−aluminum joint to form two different fracture modes: fracture at the weld and fracture at the heat affected zone.

With the increase of the aluminum's penetration depth, the tensile resistance increased accordingly. However, the occurrence of the fracture in the heat affected zone resulted in a decrease in tensile resistance. Therefore, the analyses of the influence of welding parameters on tensile resistance were carried out.

3.2 Effect of laser power on lap tensile resistance

Laser power (*P*) is an important parameter for laser welding and this parameter directly affects the energy density of the laser. In the case where the welding speed and the defocus amount are constant, the greater the laser power is, the greater the heat input (*H*) is. While the laser heat input is inversely proportional to welding speed (*S*), the greater the welding speed is, the smaller the laser heat input is. Therefore, the relationship between the laser heat input and the welding parameters, without considering the efficiency, can be expressed as follows:

$$H=P/S \tag{1}$$

The lap tensile resistance under different laser powers is shown in Fig. 3(a), and the mean value of lap tensile resistance under different laser powers is shown in Fig. 3(b). There is a parabolic relationship between the lap tensile resistance and the laser power. When the laser power was less than 1.7 kW ($H\leq$34 J/mm), the aluminum plate failed to connect

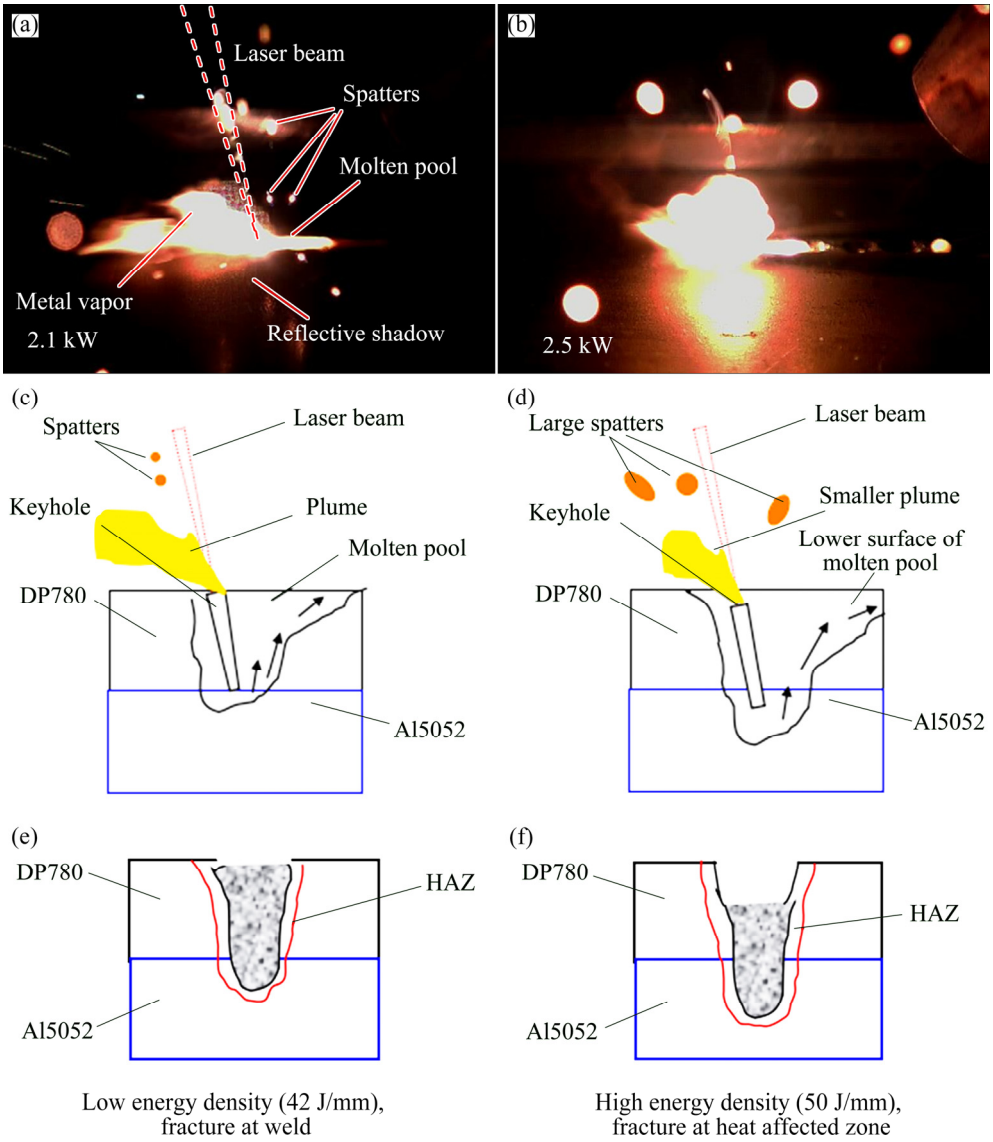

Fig. 2 Images during laser welding process (a, b) and schematic diagrams of welding process under laser powers of 2.1 kW (c, e) and 2.5 kW (d, f)

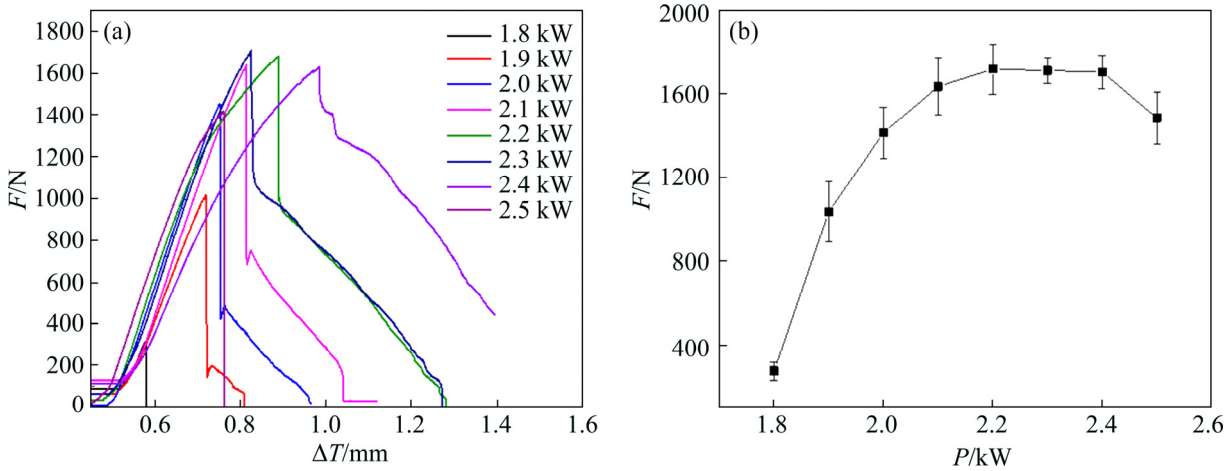

Fig. 3 Lap tensile resistance under different laser powers (a) and mean value of lap tensile resistance under different laser powers (b) (F: Lap shear force; ΔT: Tensile displacement)

with the steel plate and the welding strength was 0. When the laser power was between 1.8 to 2.1 kW (36 J/mm ≤ H ≤ 42 J/mm), the lap tensile resistance was 274 to1633 N; when the laser power was 2.2 to 2.4 kW (44 J/mm ≤ H ≤ 48 J/mm), the lap tensile resistance was relatively stable at 1633−1710 N which was the highest value; when the power was greater than 2.4 kW (H ≥ 48 J/mm), the lap tensile resistance began to decrease.

3.3 Effect of welding speed on lap tensile resistance

The lap tensile resistance under different welding speeds is presented in Fig. 4(a). The mean value of lap tensile resistance under different welding speeds is shown in Fig. 4(b). There is a linear relationship between the lap tensile resistance and the welding speed. When the welding speed was less than 2.0 m/min (H ≥ 63 J/mm), the weld seam was burnt through the specimen due to the high energy density. When the welding speed was 2.5 to 4.0 m/min (50 J/mm ≤ H ≤ 31.5 J/mm), the lap tensile resistance decreased with the increase of welding speed. The lap tensile resistance got maximum value 1964 N when the welding speed was 2.5 m/min. When the welding speed was larger than 4.5 m/min (H ≤ 28 J/mm), the aluminum plate failed to connect with the steel plate and the welding strength was 0.

3.4 Effect of defocus on lap tensile resistance

The lap tensile resistance under different defocuses (D) is shown in Fig. 5(a), and the mean value of lap tensile resistance under different defocuses is shown in Fig. 5(b). The relationship between the lap tensile resistance and focal position was an approximate parabolic relationship. As the amount of defocus increases, the lap tensile resistance increased at first and then decreased. When the defocuses were 0 and 1 mm, the lap

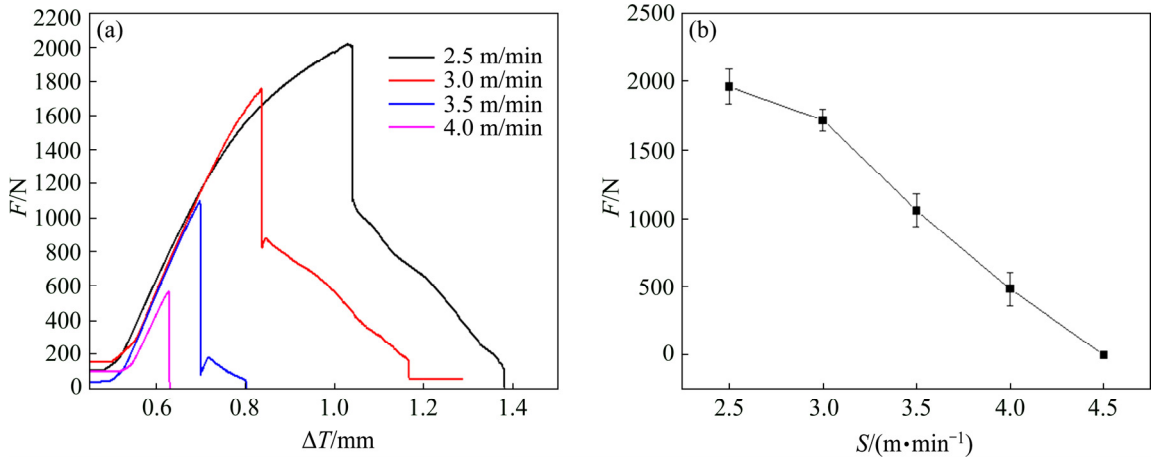

Fig. 4 Lap tensile resistance under different welding speeds (a) and mean value of lap tensile resistance under different welding speeds (b)

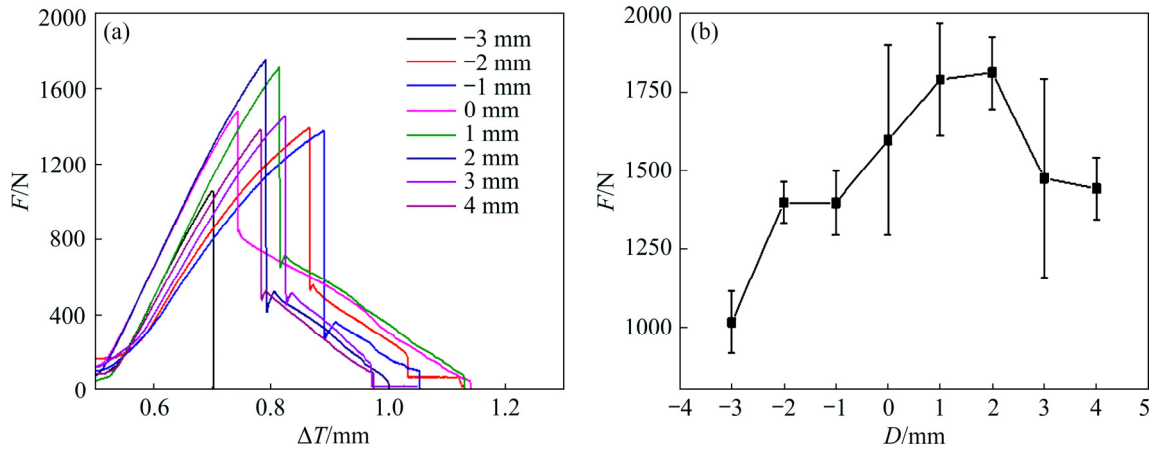

Fig. 5 Lap tensile resistance under different defocuses (a) and mean value of lap tensile resistance under different defocuses (b)

tensile resistance got a maximum value of about 1812 N; when the defocuses were −1 and 3 mm, the lap tensile resistance was about 1399 N. The standard deviation was large, which indicated that the lap tensile resistance was relatively unstable.

The intrinsic reason for the tensile resistance of steel−Al joints is probably from the weld appearance and intermetallic compounds, which is determined by the welding parameters. When the energy intensity of the laser was very low, the steel and aluminum could not be fully joined. When the energy intensity of the laser was too high, the stress and micro cracks could be increased due to the intermetallic compounds. Therefore, the stress and crack of the joint could be controlled to achieve high tensile resistance by adjusting the parameters and achieving the appropriate energy intensity.

4 Weld microstructure

4.1 Weld microstructure under different laser powers

The group test of laser power was selected to analyze the weld appearance and microstructure, which is shown in Table 2. When the laser power was 2.0−2.1 kW, the surface of the weld was full and there were no defects; when the laser power was 2.2 kW, the surface of the weld presented undercut; the width became smaller when the laser power was 2.3−2.5 kW, the steel-side surface of the weld severely sank, and the aluminum side generated a deeper penetration. So there were three kinds of weld joints: (1) the weld surface was convex, and the aluminum side generated a shallow penetration; (2) the surface of the weld slightly sank and the aluminum side generated a deep penetration; (3) the surface of the weld severely sank and the aluminum side was deeply melted. The fracture almost happened in the weld when the weld joint was class (1) or class (2), while the fracture usually happened in the HAZ when the weld joint was class (3).

Table 2 shows the value of the melting height (H_m) and the D_p under different laser powers. The effects of laser power on the H_m on the steel side and the penetration depth (D_p) on the aluminum side changed with laser powers are shown in Figs. 6(a) and (b), respectively. As the laser power increased, the value of H_m increased slightly at first and then decreased dramatically. While the the value of D_p showed an increasing trend when the laser power was increased.

4.2 Optical microstructure

Figure 7 shows the optical microstructure of a welded joint when laser power is 2.1 kW. Figures 7(b) and (e) show the upper and lower parts of the weld, respectively. The martensite structure with a large grain size was formed in the fusion zone (FZ), which was symmetrically distributed and dendritic equiaxed in the center of the weld. While the base material of steel plate had a small grain size, mainly ferrite and martensite islands, which is shown in Fig. 7(c). The heat effected zone (HAZ) is shown in Fig. 7(a), which is mainly composed of tempered martensite and ferrite. Figure 7(d) shows the enlarged view of grain size of the FZ. The interaction of steel−aluminum joint is shown in Fig. 7(f). The steel−aluminum compound belt and weld defect, such as porosity can be found in Figs. 7(g−i), respectively.

Table 2 Melting height on steel side and penetration depth on aluminum side under different laser powers

P/kW	2.0	2.1	2.2	2.3	2.4	2.5
Weld appearance	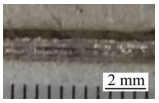	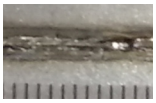			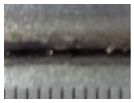	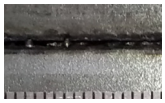
Cross section	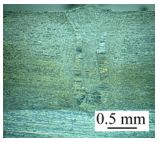	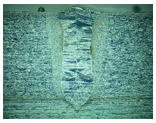	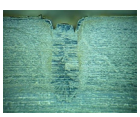			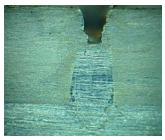
H_m/mm	0.1	0.12	−0.333	−0.884	−0.91	−0.78
D_p/mm	0.105	0.281	0.31	0.21	0.38	0.54

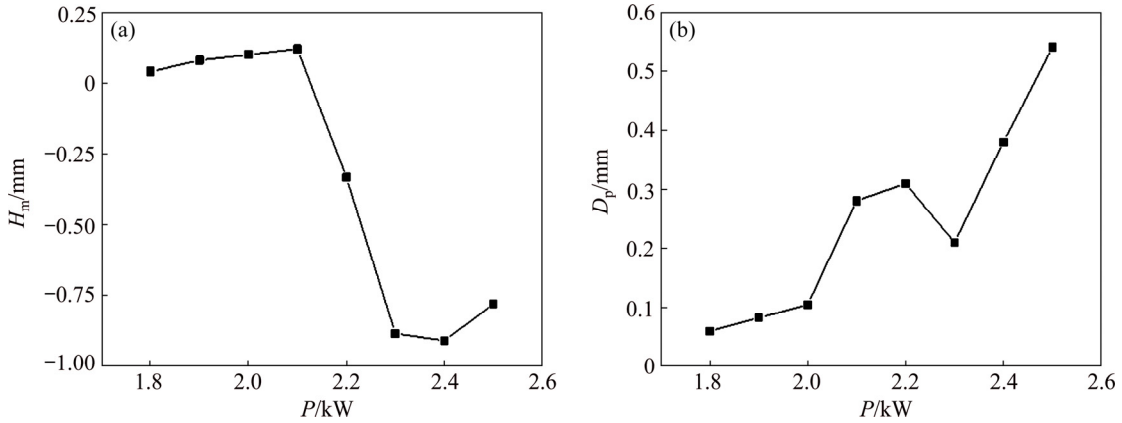

Fig. 6 Melting height (H_m) on steel side (a) and penetration depth (D_p) on aluminum side (b) under different laser powers

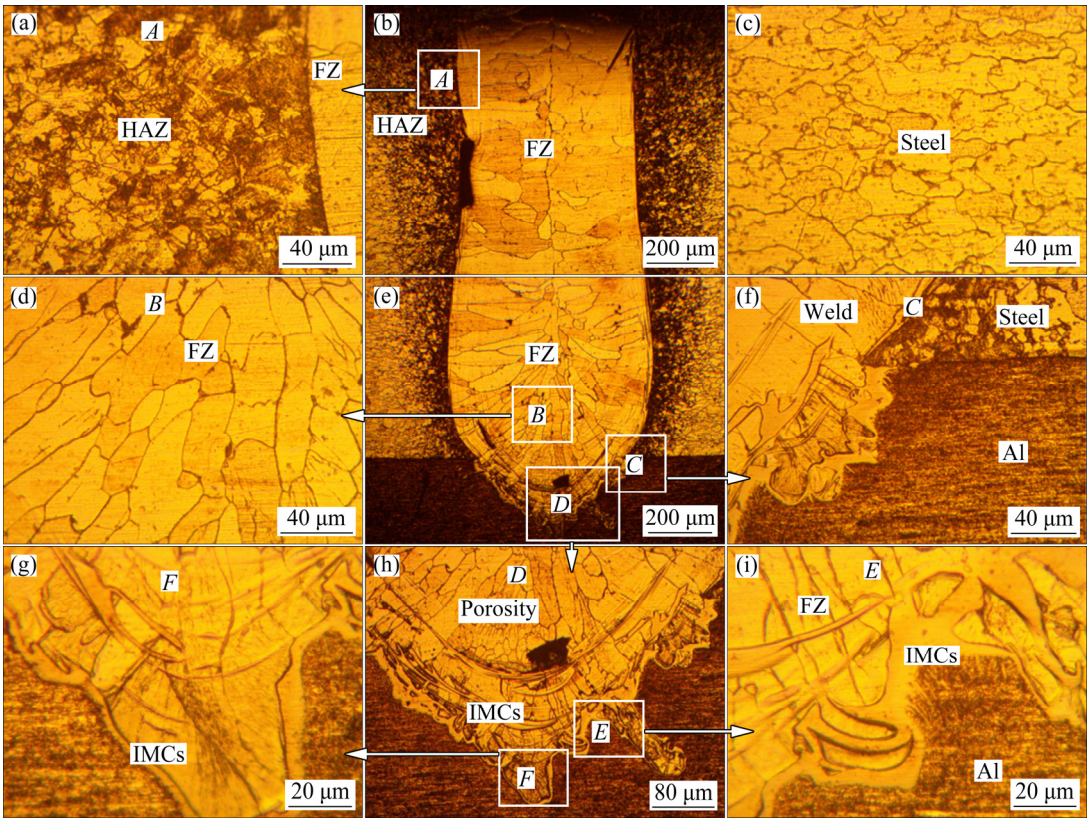

Fig. 7 Optical metallographic images of steel−aluminum joint at laser power of 2.1 kW: (a) HAZ; (b) Upper part of joint; (c) Steel; (d) Area *B* in (e); (e) Lower part of joint; (f) Area *C* in (e); (g) Area *F* in (h); (h) Steel/Al interface; (i) Area *E* in (h)

5 Intermetallic compounds and fracture mode

5.1 Formation of intermetallic compounds

The morphology and composition of iron−aluminum compounds have a very important relationship to the bonding strength of steel and aluminum. So, a comprehensive scanning electron microscope observation of the steel−aluminum interface is necessary. Figure 8 shows the SEM images of a welded joint when laser power is 2.1 kW. The enlarged views of the areas *A*, *B*, *C*, *D*, *E*, *F* and *G* are shown in Figs. 8(a, b, c, d, f, g, h, i), respectively. Figures 8(a) and (c) show the combination interface of steel, aluminum and FZ. The IMCs and martensite island are shown in Figs. 8(b), (g) and (h). Lath-shaped steel−aluminum

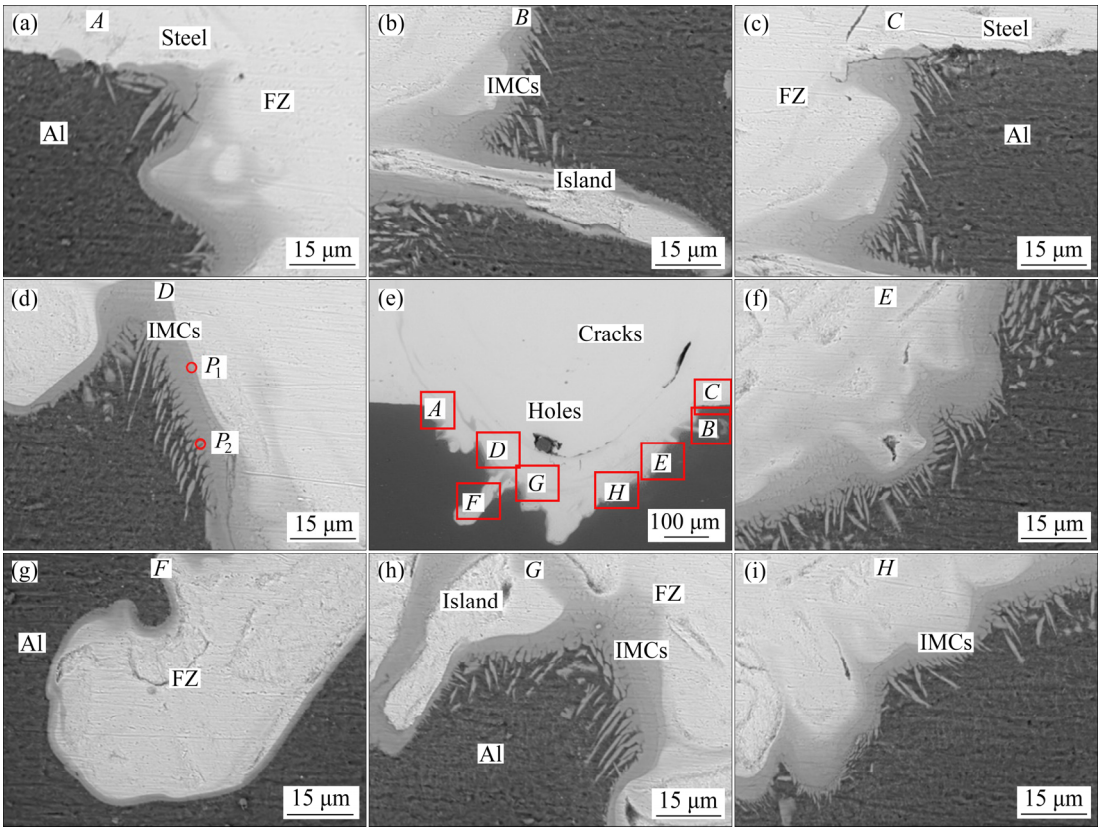

Fig. 8 SEM images of steel−aluminum joint at laser power of 2.1 kW: (a, b, c, d) Areas *A*, *B*, *C* and *D* in (e); (e) Steel/Al interface; (f, g, h, i) Areas *E*, *F*, *G*, *H* in (e)

compound bands and needle-like compounds were formed on the steel−aluminum bonding surface, which could be found in Figs. 8(d), (f), (h) and (i). The macro picture of the steel−aluminum bonding interface is shown in Fig. 8(e), and the cracks and hole could be observed in the welded arc band. To analyze the IMCs layer, the energy-dispersive X-ray spectrometer (EDS) analyses were performed at P_1 and P_2, which are shown in Fig. 8(d). The EDS results of P_1 showed that they had the chemical composition of 62.39% Al and 37.61% Fe, which corresponded to the possible phases of $FeAl_2$ and Fe_2Al_5. The EDS results of P_2 showed that they had the chemical composition of 75.89% Al and 24.11% Fe, which was identified as $FeAl_3$. Strip-shaped steel−aluminum compound bands may be composed of $FeAl_2$ and Fe_2Al_5, while the needle-like compounds mainly may be composed of $FeAl_3$. The delamination of iron−aluminum compounds can be clearly observed in Figs. 8(d) and (h), which has been reported in Ref. [31].

5.2 Fracture analysis of two failure modes

The fracture mode can reflect the mechanical properties of structural parts. With the change of inputted laser thermal energy input, the fracture mode of steel and aluminum welds can be roughly divided into two classes. When the laser energy input was moderate (laser power was 2.1 kW), both small depression on the surface of the weld seam and large penetration depths were achieved. In this way, the bonding force between steel and aluminum was greater, the strength of the heat affected zone on the steel side was higher, and the fracture occurred at the bottom of the weld seam. When the laser energy input was too high (laser power was 2.5 kW), a large depression appeared on the surface of the weld and the penetration depth was increased. In this way, the bonding force between steel and aluminum was greater, but the strength of the heat affected zone on the steel side was reduced, and the fracture occurred in the HAZ of the steel side. The comparison of the two fracture modes and the photos of the fractured part are shown in Fig. 9.

The macro picture and micrograph of the broken positions 1, 2, and 3 are shown in Fig. 10. The steel side of the broken position 1 at the failure

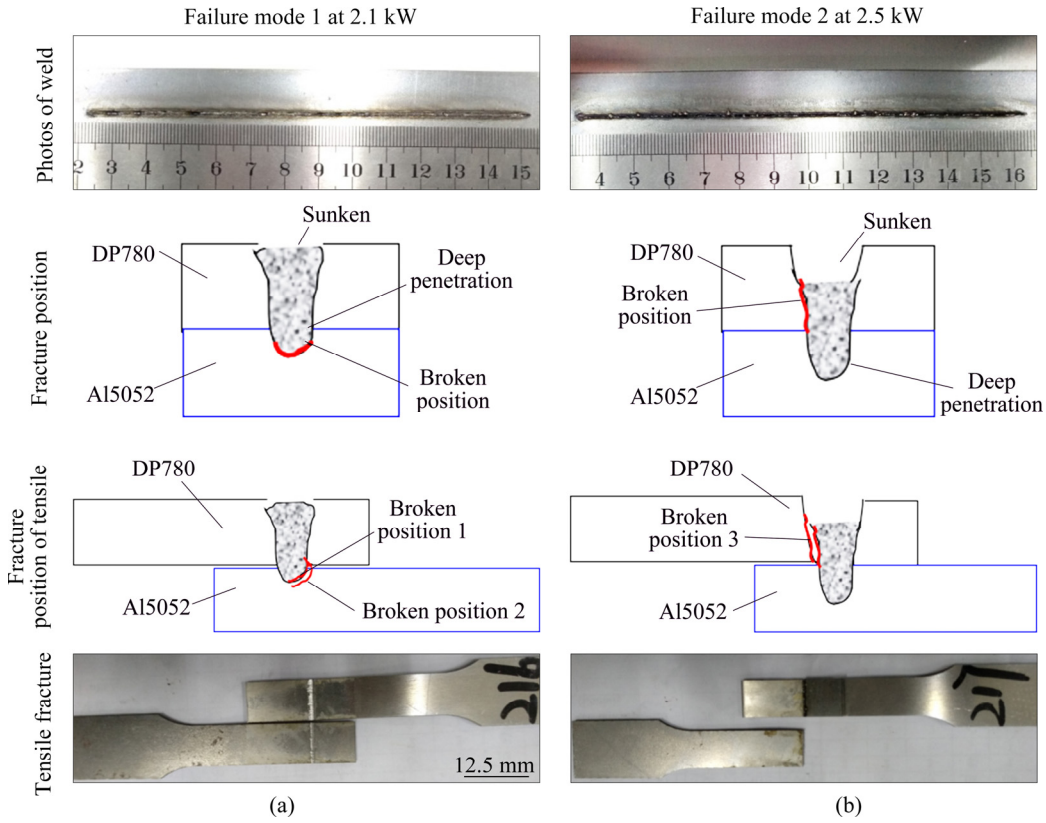

Fig. 9 Fracture position and tensile fracture of failure mode 1 (a) and failure mode 2 (b)

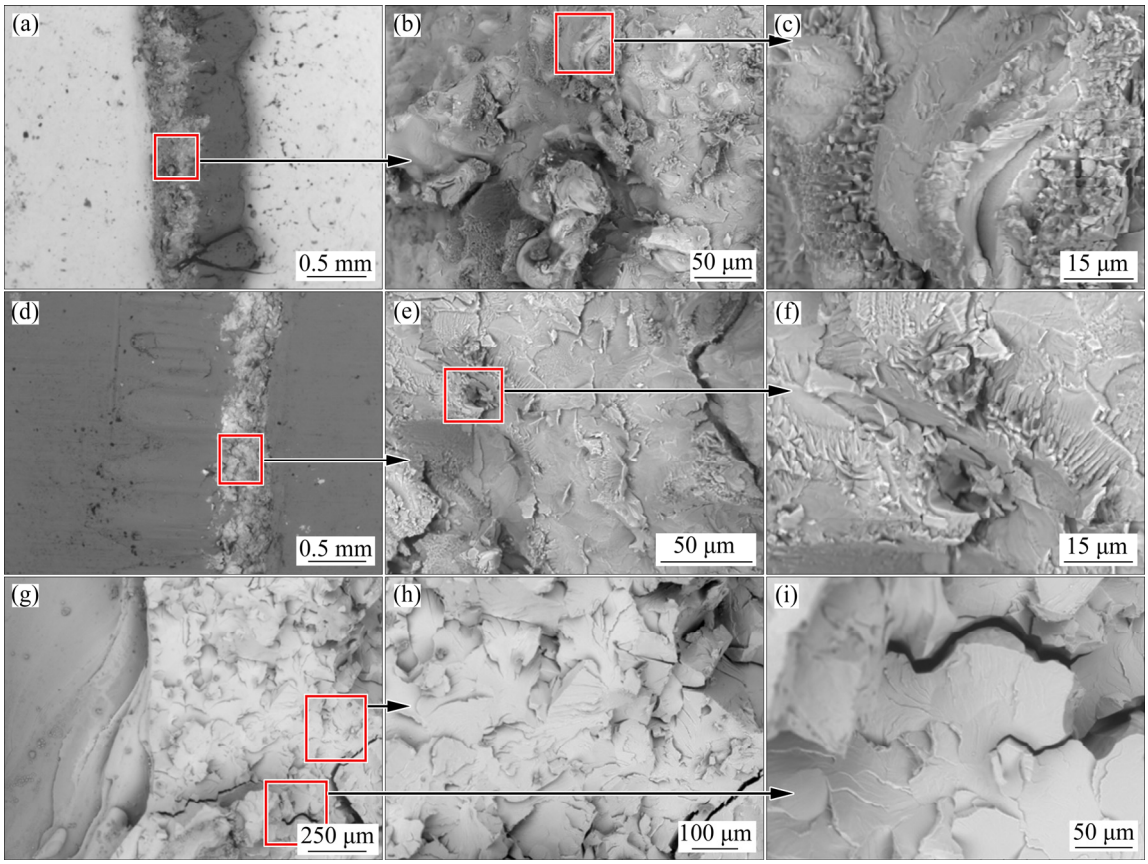

Fig. 10 SEM images of tensile fracture: (a, b, c) Steel side of broken position 1 of failure mode 1; (d, e, f) Al side of broken position 2 of failure mode 1; (g, h, i) HAZ of steel side of broken position 3 of failure mode 2

model 1 is shown in Figs. 10(a−c). The lath-shaped compounds could be observed in the micrograph. The Al side of broken position 2 at failure mode 1 is shown in Figs. 10(d−f). The cracks and needle-like compounds could be founded accordingly. This indicates that the failure happened in the IMCs. As shown in Figs. 10(g−i), the HAZ of steel side of broken position 3 is smooth. There are several secondary cracks which might be caused by the fracture. The image of the fracture surface shows that both fracture modes are brittle fractures.

6 Conclusions

(1) When the defocus is 2 mm and the laser heat inputs are 44 to 50 J/mm, a relatively stable and high joint strength can be obtained. The best lap tensile resistance reaches 1964 N, while excessive laser energy input can cause defects such as pores and blowout.

(2) The IMCs are distributed in bands at the steel−aluminum interface, including the lath-shaped band, needle-like compounds and islands. And there are delaminations in the IMCs, which has an important effect on the fracture mode of the weld.

(3) The failure mode is determined by laser line energy input and the focal position, and two kinds of failure modes are proposed. The morphology of needle-like compounds can be found on fracture micrograph.

Acknowledgments

Many thanks are given to Su-juan WANG, Lu LIANG and Zheng-rong ZHANG of Guangdong University of Technology, for their assistance of experiments.

References

[1] XUE Jun-yu, LI Yuan-xing, CHEN Hui, ZHU Zong-tao. Wettability, microstructure and properties of 6061 aluminum alloy/304 stainless steel butt joint achieved by laser-metal inert-gas hybrid welding-brazing [J]. Transactions of Nonferrous Metals Society of China, 2018, 28: 1938−1946.

[2] LI Chun-ling, FAN Ding, YU Xiao-quan, HUANG Jian-kang. Residual stress and welding distortion of Al/steel butt joint by arc-assisted laser welding-brazing [J]. Transactions of Nonferrous Metals Society of China, 2019, 29: 692−700.

[3] WANG Peng-fei, CHEN Xi-zhang, PAN Qiu-hong, MADIGAN B, LONG Jiang-qi. Laser welding dissimilar materials of aluminum to steel: an overview [J]. International Journal of Advanced Manufacturing Technology, 2016, 87: 3081−3090.

[4] MECO S, PARDAL G, GANGULY S, WILLIAMS S, MCPHERSON N. Application of laser in seam welding of dissimilar steel to aluminium joints for thick structural components [J]. Optics and Lasers in Engineering, 2015, 67: 22−30.

[5] WANG Chun-ming, CUI Ling-yue, MI Gao-yang, JIANG Ping, SHAO Xin-yu, RONG You-min. The influence of heat input on microstructure and mechanical properties for dissimilar welding of galvanized steel to 6061 aluminum alloy in a zero-gap lap joint configuration [J]. Journal of Alloys and Compounds, 2017, 726: 556−566.

[6] SUN Jun-hao, HUANG Jian, YAN Qi, LI Zhu-guo. Fiber laser butt joining of aluminum to steel using welding-brazing method [J]. International Journal of Advanced Manufacturing Technology, 2016, 85(9−12): 2639−2650.

[7] ZHOU D, LIU J, LU Y, XU S. Effect of adding powder on joint properties of laser penetration welding for dual phase steel and aluminum alloy [J]. Optics and Laser Technology, 2017, 94: 171−179.

[8] YAN Fei, FANG Xiang, CHEN Lin, WANG Chun-ming, ZHAO Juan, CHAI Fang, WANG Wei. Microstructure evolution and phase transition at the interface of steel/Al dissimilar alloys during Nd:YAG laser welding [J]. Optics and Laser Technology, 2018, 108: 193−201.

[9] QI Xiao-dong, LIU Li-ming. Fusion welding of Fe-added lap joints between AZ31B magnesium alloy and 6061 aluminum alloy by hybrid laser-tungsten inert gas welding technique [J]. Materials & Design, 2012, 33(1): 436−443.

[10] GAO Ming, CHEN Cong, MEI Shu-wen, WANG Lei, ZENG Xiao-yan. Parameter optimization and mechanism of laser-arc hybrid welding of dissimilar Al alloy and stainless steel [J]. The International Journal of Advanced Manufacturing Technology, 2014, 74(1−4): 199−208.

[11] TABAN E, GOULD J E, LIPPOLD J C. Dissimilar friction welding of 6061-T6 aluminum and AISI 1018 steel: Properties and microstructural characterization [J]. Materials & Design, 2010, 31(5): 2305−2311.

[12] TRICARICOA L, SPINAA R, SORGENTEA D, BRANDIZZIB M. Effects of heat treatments on mechanical properties of Fe/Al explosion-welded structural transition joints [J]. Materials & Design, 2009, 30(7): 2693−2700.

[13] SHIM J Y, KANG B Y, KIM I S. Characteristics of Al/steel magnetic pulse tubular joint according to discharging time [J]. Journal of Mechanical Science and Technology, 2017, 31(8): 3793−3801.

[14] YU Hai-ping, DANG Hai-qing, QIU Ya-nan. Interfacial microstructure of stainless steel/aluminum alloy tube lap joints fabricated via magnetic pulse welding [J]. Journal of Materials Processing Technology, 2017, 250: 297−303.

[15] LI Jian-xiong, LI Huan, WEI Hui-liang, GAO Ying. Effect of torch position and angle on welding quality and welding process stability in pulse on pulse MIG welding-brazing of aluminum alloy to stainless steel [J]. International Journal of Advanced Manufacturing Technology, 2016, 84(1−4): 705−716.

[16] CUI Li, CHEN Bo-xu, CHEN Li, HE Ding-yong. Dual beam laser keyhole welding of steel/aluminum lapped joints [J].

Journal of Materials Processing Technology, 2018, 256: 87−97.

[17] INDHU R, SOUNDARAPANDIAN S, VIJAYARAGHAVAN L. Yb:YAG laser welding of dual phase steel to aluminium alloy [J]. Journal of Materials Processing Technology, 2018, 262: 411−421.

[18] GUAN Qian-qian, LONG Jiang-qi, YU Ping, JIANG Shun-chao, HUANG Wen-hao, ZHOU Jian-xi. Effect of steel to aluminum laser welding parameters on mechanical properties of weld beads [J]. Optics and Laser Technology, 2019, 111: 387−394.

[19] LONG Jiang-qi, HUANG Wen-hao, XIANG Jia-wei, GUAN Qian-qian, MA Zheng-wei. Parameter optimization of laser welding of steel to Al with pre-placed metal powders using the Taguchi-response surface method [J]. Optics and Laser Technology, 2018, 108: 97−106.

[20] YAN Fei, WANG Xian-wei, CHAI Fang, MA Hui-juan, TIAN Lin-li, DU Xiao-zhong, WANG Chun-ming, WANG Wei. Improvement of microstructure and performance for steel/Al welds produced by magnetic field assisted laser welding [J]. Optics and Laser Technology, 2019, 113: 164−170.

[21] PEREIRA A B, CABRINHA A, ROCHA F, MARQUES P, FERNANDES F A O, de SOUSA R J A. Dissimilar metals laser welding between DP1000 steel and aluminum alloy 1050 [J]. Metals, 2019, 9(1): 102.

[22] NIROUMAND-JADIDI A, KASHANI-BOZORG S F. Microstructure and property assessment of dissimilar joints of 6061-T6 Al/dual-phase steel fabricated by friction stir spot welding [J]. Welding in the World, 2018, 62: 751−765.

[23] YE Zheng, HUANG Ji-hua, CHENG Zhi, XIE Li, ZHANG Yu-feng, CHENG Shu-hai, YANG Jian. Study on butt joining 5052 aluminum alloy/Q235 mild steel by MIG−TIG double-sided arc welding-brazing process [J]. Welding in the World, 2018, 62: 145−154.

[24] MEI S, GAO M, YAN J, ZHANG C, LI G, ZENG X. Interface properties and thermodynamic analysis of laser-arc hybrid welded Al/steel joint [J]. Science and Technology of Welding and Joining, 2013, 18(4): 293−300.

[25] YANG Jin, LI Yu-long, ZHANG Hua, GUO Wei, WECKMAN D, ZHOU N. Dissimilar laser welding/ brazing of 5754 aluminum alloy to DP 980 steel: Mechanical properties and interfacial microstructure [J]. Metallurgical and Materials Transactions A, 2015, 46(11): 5149−5157.

[26] CHEN Nan-nan, WANG Min, WANG Hui-ping, WAN Zi-xuan, CARLSON B E. Microstructural and mechanical evolution of Al/steel interface with Fe_2Al_5 growth in resistance spot welding of aluminum to steel [J]. Journal of Manufacturing Processes, 2018, 34: 424−434.

[27] TAN Cai-wang, ZANG Cheng-wei, XIA Hong-bo, ZHAO Xiao-ye, ZHANG Kai-ping, MENG Sheng-hao, CHEN Bo, SONG Xiao-guo, LI Li-qun. Influence of Al additions in Zn-based filler metals on laser welding–brazing of Al/steel [J]. Journal of Manufacturing Processes, 2018, 34: 251−263.

[28] LIU Gui-qian, GAO Xiang-dong, YOU De-yong, ZHANG Nan-feng. Prediction of high power laser welding status based on PCA and SVM classification of multiple sensors [J]. Journal of Intelligent Manufacturing, 2019, 30: 821−832.

[29] YOU De-yong, GAO Xiang-dong, KATAYAMA S. A novel stability quantification for disk laser welding by using frequency correlation coefficient between multiple-optics signals [J]. IEEE-ASME Transactions on Mechanics, 2015, 20(1): 327−337.

[30] YOU De-yong, GAO Xiang-dong, KATAYAMA S. WPD-PCA-based laser welding process monitoring and defects diagnosis by using FNN and SVM [J]. IEEE Transaction on Industrial Electronics, 2015, 62(1): 628−636.

[31] WANG Xiao-hong, GU Xiao-yan, SUN Da-qian. Research on interface characteristic of laser welding joints of steel/aluminum dissimilar materials [J]. Journal of Mechanical Engineering, 2017, 53(4): 26−33. (in Chinese)

钢/铝激光搭接焊接头的抗拉强度、显微组织及断裂模式

刘桂谦，高向东，彭 聪，刘秀航，黄怡洁，张艳喜，游德勇

广东工业大学 广东省焊接工程技术研究中心，广州 510006

摘 要：通过激光搭接焊实现 5052 铝合金与 DP780 双相钢异种金属的连接。对焊接过程的金属蒸气和飞溅进行高速摄像检测，并利用万能试验机对焊接接头进行力学性能测试，分析搭接剪切力随激光焊接参数的变化规律。分别采用光学显微镜和扫描电子显微镜对样品进行表征。通过显微组织观察发现在钢/铝界面形成 3 种不同的金属间化合物相，即带状 Fe_2Al_5、$FeAl_2$ 和针状 $FeAl_3$，探索在不同的激光热量输入下，搭接抗拉强度、激光参数和失效断裂模式之间的关系。结果表明，钢/铝接头在低热量输入和高热量输入出现两种不同的断裂模式，分别为沿焊缝热影响区和沿铝钢接合界面断面，并均为脆性断裂。此外，发现断裂界面都出现裂纹，且在断裂的微观形态中生成针状簇。

关键词：激光搭接焊；抗拉强度；显微组织；断裂模式

(Edited by Xiang-qun LI)